Differences of Rainfall Estimates over Land by Tropical Rainfall Measuring Mission (TRMM) Precipitation Radar (PR) and TRMM Microwave Imager (TMI)—Dependence on Storm Height

FUMIE A. FURUZAWA AND KENJI NAKAMURA

Hydrospheric Atmospheric Research Center, Nagoya University, Nagoya, Japan

(Manuscript received 29 December 2003, in final form 19 August 2004)

ABSTRACT

It is well known that precipitation rate estimation is poor over land. Using the Tropical Rainfall Measuring Mission (TRMM) precipitation radar (PR) and TRMM Microwave Imager (TMI), the performance of the TMI rain estimation was investigated. Their differences over land were checked by using the orbit-by-orbit data for June 1998, December 1998, January 1999, and February 1999, and the following results were obtained: 1) Rain rate (RR) near the surface for the TMI (TMI-RR) is smaller than that for the PR (PR-RR) in winter; it is also smaller from 0900 to 1800 LT. These dependencies show some variations at various latitudes or local times. 2) When the storm height is low (<5 km), the TMI-RR is smaller than the PR-RR; when it is high (>8 km), the PR-RR is smaller. These dependencies of the RR on the storm height do not depend on local time or latitude. The tendency for a TMI-RR to be smaller when the storm height is low is more noticeable in convective rain than in stratiform rain. 3) Rain with a low storm height predominates in winter or from 0600 to 1500 LT, and convective rain occurs frequently from 1200 to 2100 LT. Result 1 can be explained by results 2 and 3. It can be concluded that the TMI underestimates rain with low storm height over land because of the weakness of the TMI algorithm, especially for convective rain. On the other hand, it is speculated that TMI overestimates rain with high storm height because of the effect of anvil rain with low brightness temperatures at high frequencies without rain near the surface, and because of the effect of evaporation or tilting, which is indicated by a PR profile and does not appear in the TMI profile. Moreover, it was found that the PR rain for the cases with no TMI rain amounted to about 10%–30% of the total but that the TMI rain for the cases with no PR rain accounted for only a few percent of the TMI rain. This result can be explained by the difficulty of detecting shallow rain with the TMI.

1. Introduction

Precipitation is one of the major components of the earth's climate system. Precipitation is a result of water vapor condensation, which is caused by many factors such as water vapor convergence, updraft, radiation, orography, surface evapotranspiration, and so on. On the other hand, the total amount of precipitation provides an amount of latent heat release to the atmosphere. This heating is one of the strongest driving forces of the atmospheric general circulation. Precipitation is also very crucial for humans. For almost all countries, precipitation is the main source of freshwater. The prediction of the variation of the precipitation distribution that is associated with the recent global warming is recognized as an important issue.

One of the major difficulties in measuring precipitation arises from its regional and temporal variations. These variations are significant obstacles for the precise measurement of precipitation. In addition, over vast oceans, tropical rain forests, or remote areas, precipitation measurements are very scarce. Thus, the precise measurement of global precipitation is a challenge. The Tropical Rainfall Measuring Mission (TRMM), which is a joint venture between the United States and Japan, is aimed to meet that need. TRMM was originally designed to measure rain over the tropical and subtropical regions, where more than two-thirds of global precipitation occurs (Simpson et al. 1988). A unique aspect of TRMM is that it is equipped with a precipitation radar (PR). Before TRMM, there was no spaceborne rain radar, and global precipitation observation was conducted with visible/infrared radiometers on geostationary satellites such as the Geostationary Operational Environmental Satellites, Geostationary Meteorological Satellites or Meteosats, or polar-orbiting satellites like the National Oceanic and Atmospheric Administration series. Another sensor used before TRMM is the microwave radiometer. The well-known Special Sensor Microwave Imagers (SSM/I) on the U.S. De-

Corresponding author address: Fumie A. Furuzawa, Hydrospheric Atmospheric Research Center, Nagoya University, Furocho, Chikusa-ku, Nagoya 464-8601, Japan.
E-mail: akimoto@hyarc.nagoya-u.ac.jp

fense Meteorological Satellite Program satellites currently continuously provide valuable data. Microwave radiometers measure brightness temperature emitted or scattered by the precipitation system, whereas the visible/infrared measurement is indirect because visible/infrared radiometers observe clouds instead of rain. The rain radar measurement has a very high accuracy, whether taken over land or ocean, and it is independent of other measurements. TRMM has not only the radar (PR) but also a microwave radiometer [TRMM Microwave Imager (TMI)] and a visible/infrared radiometer (Visible and Infrared Scanner). These sensors observe a rain system nearly simultaneously, that is, within less than 1 min because of the difference in the scan geometries. The quasi-simultaneous measurement gave us a significant opportunity to improve the rain intensity estimates by radiometers and rain radars.

The rain estimation algorithm for the PR is described by Iguchi et al. (2000). The PR operates at a frequency of 14 GHz, which suffers from rain attenuation. The rain-attenuation correction is one of the major tasks of the PR algorithm. When rain is weak, an iteration method based on the Hitschfeld–Bordan method (Hitschfeld and Bordan 1954) is applied. When rain is intense and the rain attenuation is high, a surface reference technique (Meneghini et al. 2000) is applied. A beam-filling correction is also incorporated. The so-called reflectivity–rain-rate (Z–R) relationship is still a significant issue for rain estimation. The microwave radiometer rain estimation algorithm is based on model simulation results (e.g., Kummerow and Giglio 1994). Using the results of a cumulus ensemble model, brightness temperatures for each TMI channel are calculated to generate a lookup table. The most suitable precipitation structure is determined by a Bayesian technique from the measured brightness temperatures (Kummerow et al. 2001).

The rain estimation algorithms are different between the TMI and PR. The difference of their retrieved rain rates (RRs) helps to improve the algorithms. For example, Masunaga et al. (2002) and Ikai and Nakamura (2003) pointed out that the rain height that is assumed in the TMI rain estimation algorithm has a problem. Over the ocean, the brightness temperatures at low frequencies increase when rain exists. This effect is because of the emission from rain in addition to the background emission from the ocean surface, water vapor, or, in some cases, from cloud water. Rain estimation by the TMI over land is a difficult task. There are some regions for which the surface emission is larger than that from rain. Even more serious is that the surface emission has large regional and temporal variabilities. Therefore, the emission from rain is difficult to distinguish from the surface emission. Thus, the so-called scattering mode is explicitly or implicitly used. When a high cloud system exists, the ice particles in the upper part of the system scatter the microwaves emitted from the surface and the rain layer, resulting in a cold brightness temperature at high frequencies (Spencer et al. 1989; Spencer 1986). Because high clouds are usually associated with intense rain, the reduction of the brightness temperatures by the scattering at high frequencies can be associated with rain intensity. Thus, the rain estimation may be good for high cloud systems but may not be so accurate for low cloud systems. The rain estimates over land by the TMI, however, are not so different from those by the PR (Kummerow et al. 2000), which may be partly because rain over land is generally associated with high clouds. Nevertheless, shallow precipitation does commonly appear over land, for example, orographic rain, even though the contribution to the rain total might be small. The bias of the microwave rain estimates for the shallow precipitation systems may be more crucial for the study of the diurnal variation of rain over land.

This paper is focused on the instantaneous rain estimation differences between the PR and TMI over land at high spatial resolution, where the rain height and rain type were taken into consideration. Because of its range-resolution capability, the PR measures the rain height, and we can stratify the rain systems according to rain height in addition to rain type. Results of this analysis are described in section 3 and discussed in section 4. Our conclusions and summary are presented in section 5.

2. Instruments, data, and analysis

Over land, rain intensity estimates from microwave radiometers on satellites have larger errors than over the ocean, and the retrieval algorithm is not yet completely established. To search for the origin of the errors to aid in algorithm improvement, we compared the TRMM rain rates near the surface for the PR (PR-RR) and TMI (TMI-RR) over land. The TMI scanned a 759-km-wide swath in a conical manner with a viewing angle of 49° off nadir, which results in an incidence angle of 52.8° at the earth's surface. The PR scanned a 220-km-wide swath with cross-track scanning, ±17° off nadir. In this work, only the TMI data coincident with the PR were used. Though the observation time differs by about 1 min because of the different scan geometries, the time difference is negligibly small as compared with the lifetime of rain systems of about 3 h. Thus, we can ignore this difference. The PR is a radar with frequencies of 13.796 and 13.802 GHz, and the TMI is a passive detector (radiometer) with nine channels: horizontal and vertical polarizations at 10.7, 19.4, 37.0, and 85.5 GHz and only vertical polarization at 21.3 GHz. A detailed description of the TRMM spaceborne sensor package is given in Kummerow et al. (1998). The physical processes used for rain retrieval of the TMI and PR are different. Surface background radiation has an impact on the TMI retrievals, whereas there is little or no impact on the PR. On the other hand, the PR-RR

is estimated by using raindrop size distributions obtained by α adjustment method based on assumed raindrop size distributions that are appropriate for convective and stratiform rain (Iguchi et al. 2000). This drop size distribution varies significantly depending on, for example, orographic conditions. It is not known whether this is always suitably estimated.

We analyzed the level-2 data of the TRMM standard products, version 5 (Kummerow et al. 2001; Ferraro 1997), for June and December of 1998 and January and February of 1999. These data were produced by the U.S. National Aeronautics and Space Administration (NASA) and the National Space Development Agency of Japan [now the Japan Aerospace Exploration Agency (JAXA)]. Level-2 data include meteorological parameters such as rain rate, storm height, freezing height, and rain type. We used rain rates near the surface and at each altitude in TMI-2A12 and PR-2A25 and storm height and rain type (convective/stratiform/others, warm rain) in PR-2A23. Here, the near-surface rain is defined as the rain at the lowest height of the surface that is free from sidelobe-coupled surface signal clutter arising from surface topography.

Land/ocean/coastline classification was done using the surface flag for the TMI and the method flag for the PR. We divided the TMI and PR data into three groups by using these flags. Data for which the TMI and PR had the same surface classification were used for our analysis. Events flagged as being "rain certain" for the PR data and "rain possible" for the TMI data were selected. These screening procedures were performed on the TRMM orbital data. The data were then gridded at a resolution of 0.2° of latitude and longitude for each pass and each local time. Each grid box contained roughly 20 PR and 10 (high frequency) TMI footprints.

For comparison of the TRMM PR and TMI rain rates near the surface, histograms of $\log_{10}$(TMI-RR/PR-RR) were made for each local time, latitude, and storm height, respectively. Here, the common logarithm is adopted to handle the TMI-RR and PR-RR equally and to handle a wide range of ratio. The step of the histograms $\delta \log_{10}$(TMI-RR/PR-RR) is 0.04; that is, the ratio TMI-RR/PR-RR is logarithmically spaced by a factor of 1.1 (see Figs. 1, 4, 8, 9, and 11 below). By fitting the histograms with a Gaussian distribution, we tried to quantify the trend of differences between the TRMM PR-RR and TMI-RR from the central position of the Gaussian profile (as in Fig. 1 below).

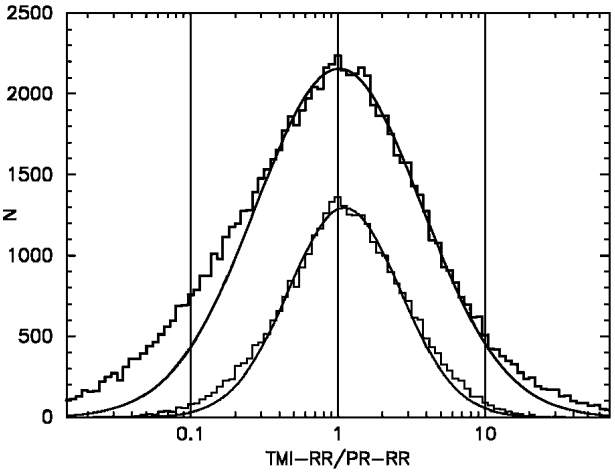

FIG. 1. Histograms of the ratio TMI-RR/PR-RR over land between 37°S and 37°N in Jun 1998. The x-axis step of the histogram is logarithmically spaced by a factor of 1.1. The thick step line is a histogram for all pixels, and the thin step line is for pixels with TMI-RR and PR-RR of >0.7 mm h^{-1}. Gaussian models are fitted within the range TMI-RR/PR-RR from -0.32 to 3.2. The parameters for the Gaussian model shown by the thick line are as follows: the central position of the $\log_{10}$(TMI-RR/PR-RR) is 0.003 ± 0.009 (i.e., TMI-RR is 0.7% larger than PR-RR), the width of the $\log_{10}$(TMI-RR/PR-RR) is 0.58 ± 0.02, and the normalization is 2146 ± 24. For the model shown by the thin line, they are 0.04 ± 0.01, 0.38 ± 0.01, and 1294 ± 23, respectively.

3. Results

a. Overall view of TMI rain bias over land

A histogram of the TMI-RR/PR-RR was obtained from the global gridded data for June 1998 to study the relationship of the TMI-RR and PR-RR over land, which is shown by a thick step line in Fig. 1. The thick solid line in this figure shows the best-fitted Gaussian profile within the $\log_{10}$(TMI-RR/PR-RR) from -0.5 to 0.5. The Gaussian profile is extrapolated outside of the fitting region. At first glance, the histogram seems to be symmetric and well fitted by a Gaussian profile. An unbiased correlation between TMI-RR and PR-RR is achieved. This histogram indicates that the TMI and PR very often retrieve consistent rain rates over land. At the lower edge of this histogram, however, one can notice a difference from the Gaussian profile. This histogram shows that TMI-RR frequently has a lower value than does PR-RR at TMI-RR/PR-RR of less than 0.25. If we limit our analysis to those cases in which both the TMI-RR and the PR-RR are greater than 0.7 mm h^{-1} (the minimum detectable rain rate for the PR), the histogram is shown by the thin step line results. Here this asymmetry appears to be very weak. Therefore, it is evident that this excess generally occurs when the pixels have a TMI-RR or PR-RR of less than 0.7 mm h^{-1}.

We studied the dependencies of the central position of a histogram for the TMI-RR/PR-RR on zonal regions and local time for June of 1998 and for December 1998–February 1999. After the histograms were made at various zonal regions and various local times, Gaussian profiles were fitted within the range of the $\log_{10}$(TMI-RR/PR-RR) from -1.9 to 1.9. This wide range of the x axis is selected to include the influence of the excess at the lower edge of the x axis, as shown in Fig. 1. The best-fit parameters and errors (1 σ, or standard deviation) of the center values of Gaussian profiles at each zonal region and each local time are plot-

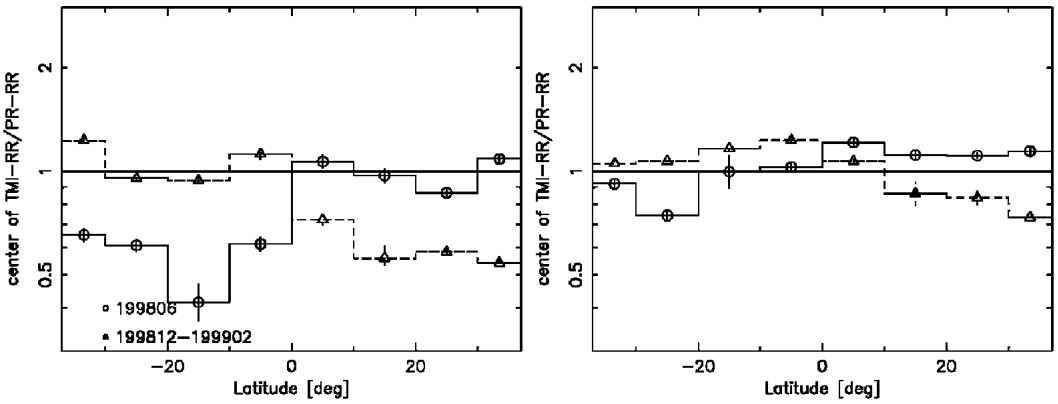

FIG. 2. Dependence of the distributions of TMI-RR and PR-RR on latitude over land. The ordinate is the peak position of the Gaussian model that fits the histogram of the $\log_{10}$(TMI-RR/PR-RR). The abscissa is latitude. Data are for Jun 1998 (open circles and solid line) and for Dec 1998–Feb 1999 (open triangles and dashed line). (left) All pixels; (right) pixels with TMI-RR and PR-RR of >0.7 mm h^{-1}. Error bars are 1 σ.

ted in Figs. 2 and 3, respectively. The left panel in Fig. 2 shows the dependence on latitude. In boreal summer, shown by open circles, the TMI-RR/PR-RR is nearly unity in the Northern Hemisphere, but it is lower than unity in the Southern Hemisphere. In boreal winter (open triangles), the TMI-RR/PR-RR is nearly unity in the Southern Hemisphere, but it is lower than unity in the Northern Hemisphere. These results mean that the TMI-RR is smaller than PR-RR in the winter area and that the TMI-RR is frequently consistent with PR-RR in the summer area. Even if both the TMI-RR and PR-RR are selected to be larger than 0.7 mm h^{-1}, these dependencies show the same tendency (as shown in the right panel of Fig. 2). However, the differences between the TMI-RR and PR-RR are smaller than in the case that includes weak rain in the winter. The TMI-RR is only 60%–80% of the PR-RR. On the other hand, in the summer, the differences become larger and the TMI-RR is 1.1 times the PR-RR.

Moreover, the dependence on local time (Fig. 3) makes it clear that the TMI-RR is smaller than the PR-RR in the daytime. This period of lower TMI-RR lasts from 0600 to 1800 LT in June (open circles) and from 0900 to 1800 LT from December to February (open triangles). When the TMI-RR and PR-RR are both selected to be larger than 0.7 mm h^{-1}, these dependencies show the same tendency but the differences between the TMI-RR and PR-RR decrease from a ratio of 0.6 to a ratio of 0.9 in the daytime and increase from a ratio of 1.1 to a ratio of 1.3 at night (not shown). The dependencies on latitude and local time show some variation at various latitudes or local times (not shown). Figures 2 and 3 indicate that we must be careful when comparisons among regions with different latitude or diurnal variations are studied, because the differences between the TMI-RR and PR-RR are obviously important.

Next, we focus on the storm height SH, because SH is a key implicit parameter included in the database used to retrieve the TMI-RR (Ikai and Nakamura 2003; Masunaga et al. 2002). Figure 4 shows histograms of the TMI-RR/PR-RR for each storm height that is classified by the PR. It is noted that the storm height depends on the size of frozen hydrometeors because of the sensitivity of the 13.8-GHz radar echoes to ice. In Fig. 4, histograms for June of 1998 are shown by solid step lines, and those from December of 1998 to February of 1999 are shown by dotted step lines. All of the histograms are symmetric and seem to be congruent. When the storm height is low (<5 km), the TMI-RR is smaller. On the contrary, when it is high (>8 km), then the PR-RR is smaller. Because all of the histograms are also well fitted with a Gaussian profile, the center of each histogram can be quantitatively determined. Three best-fit Gaussian parameters and their 1-σ errors are plotted in Fig. 5 (left panel). The results during the two periods are very similar. These center positions gradually change toward large TMI-RR/PR-RR as the

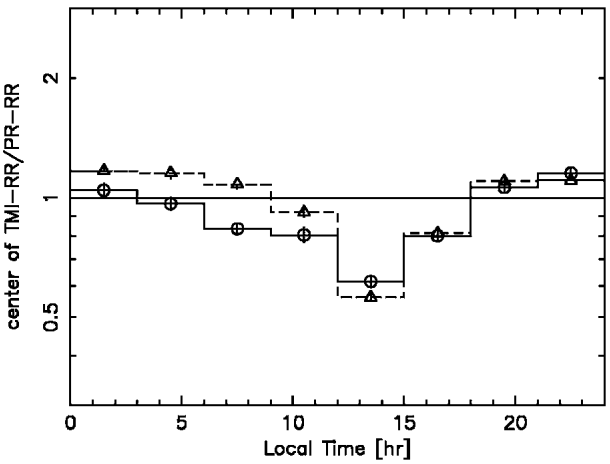

FIG. 3. Similar to Fig. 2 (left panel), but showing dependence on local time for all pixels.

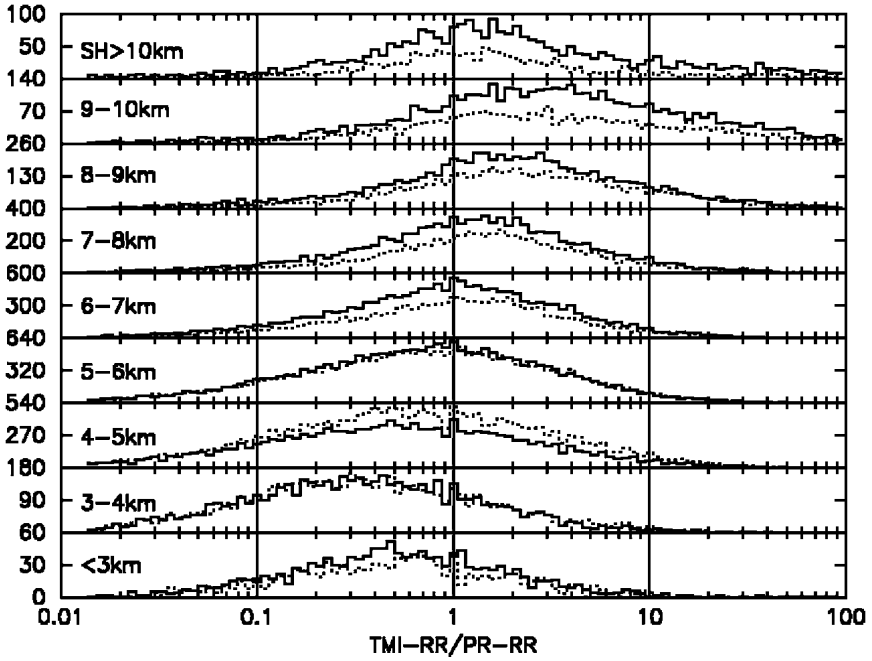

FIG. 4. Histograms of TMI-RR/PR-RR for each PR storm height over land in Jun 1998 (solid step lines) and Dec 1998–Feb 1999 (dotted step lines). The *x*-axis step of the histogram is logarithmically spaced by a factor of 1.1.

storm height becomes higher, except for histograms with storm heights lower than 3 km and higher than 10 km (Fig. 5 left-top panel). The range of the central $\log_{10}$(TMI-RR/PR-RR) values is from -0.5 to 0.5. Because many pixels have storm height of 4–7 km (as shown in the left-bottom panel of Fig. 5), small values of TMI-RR/PR-RR appear frequently. When the TMI-RR and PR-RR are selected to be larger than 0.7 mm h^{-1}, resultant parameters are shown by squares in the right panel of Fig. 5. Only June of 1998 is shown to avoid complexity. For comparison, results for the same period, but not selected by the rain-rate criterion, are also shown by circles. By this selection, a part of the events with storm heights of less than 7 km was mainly excluded, according to the right-bottom panel of Fig. 5. The center of the $\log_{10}$(TMI-RR/PR-RR) approached zero but with the same tendency, because a positive correlation is still maintained (Fig. 5 right-top panel).

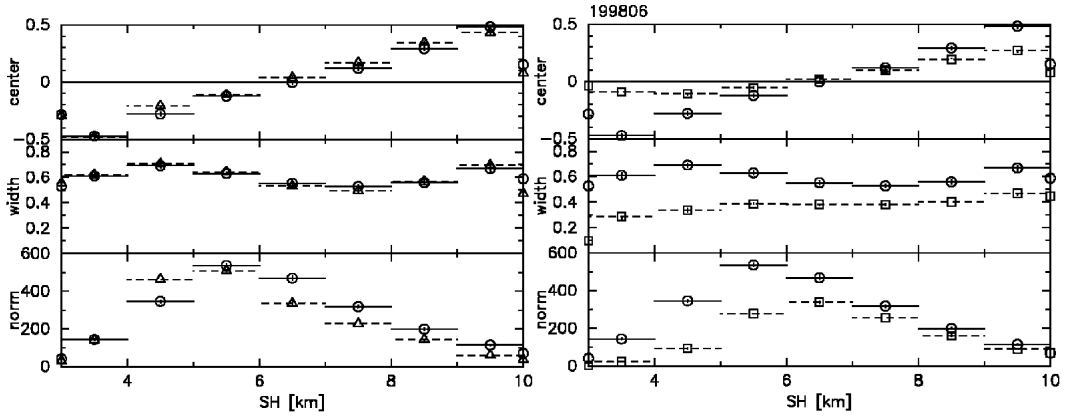

FIG. 5. (left) Best-fit parameters of Gaussian profiles for histograms shown in Fig. 4. Open circles and solid lines are for Jun 1998, and open triangles and dashed lines are for Dec 1998–Feb 1999. (right) Best-fit parameters for Jun 1998: open circles and solid lines match the left panel, and open squares and dashed lines are for the case in which both PR-RR and TMI-RR are >0.7 mm h^{-1}. (top) The value of $\log_{10}$(TMI-RR/PR-RR) for the central position of the Gaussian profile, (middle) the width, and (bottom) the normalization. Data at the SH of 3 km are for the SH of <3 km, and data at the SH of 10 km are for >10 km.

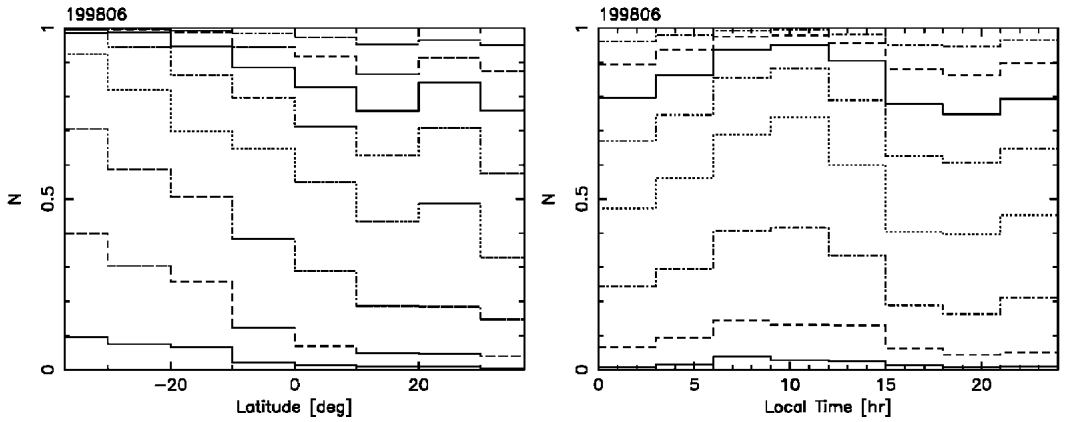

FIG. 6. Fraction of the number of rain events with storm height <3 (between zero and the lowest step line), 3–4 (between the lowest step line and a second lower step line), 4–5, 5–6, 6–7, 7–8, 8–9, 9–10, and >10 km (between the highest step line and unity) in Jun 1998: dependence on (left) latitude and (right) local time every 3 h.

The width of the Gaussian profile decreased (Fig. 5 right-middle panel), meaning that the deviation became smaller. This dependence on the storm height as shown in Figs. 4 and 5 does not depend much on the local time or the latitude (not shown). The low-storm-height case of the histograms showing different central values in the left panel of Fig. 5 is shown to be due to weak rain with RR <0.7 mm h^{-1} from the right-top panel of Fig. 5, and another origin of a decrease in central values is due to convective rain with good correlation as described in section 3c.

Figures 2–5 indicate that the global total histogram with a crude consistency between the TMI and PR as shown in Fig. 1 consists of various histograms with poor consistency. When the TMI-RR is lower than the PR-RR in Figs. 2 and 3, rain with a low storm height dominates as shown in Fig. 6. This figure shows the fraction of the number of rain events with each storm height. Shallow rain is dominant in the winter (left panel of Fig. 6), and rain with a high storm height is dominant in the summer. This pattern is consistent with Short and Nakamura (2000). The right-hand panel of Fig. 6 reveals that shallow rain is dominant from 0600 to 1500 LT. It may be because rain with a high storm height frequently develops after this period, does not dissipate, and keeps the height until morning. Instead of the number of rain events, we used the rain amount for each storm height. The result has also the same tendency as this figure (not shown). These panels suggest that the TMI-RR is too small and/or the PR-RR is too large in the winter and from 0600 to 1800 LT, because the TMI underestimates and/or the PR overestimates a rain rate with low storm height over land. The TMI-RR is generally lower than the PR-RR between 1500 and 1800 LT, but it is not due to the predominance of these shallow systems but rather to the predominance of convective rain, as discussed in section 3c.

On the other hand, for the case of a rain rate with a high storm height, because the PR may underestimate and/or the TMI may overestimate, the ratio of the TMI-RR to PR-RR is large. Masunaga et al. (2002) concluded that PR-RR underestimates at rain maximum latitude. So, a strong rain during evening with a high storm height may be underestimated by the PR. However, the possibility that the TMI may overestimate rain rate cannot be ruled out.

One of the plausible reasons may be anvil rain, that is, stratiform rain of a mesoscale convective system. Anvil rain develops in warm summer and tropical conditions from late afternoon to evening. These environmental conditions are in agreement with those showing the large ratio of TMI-RR to PR-RR. Anvil rain is formed from the mature to decaying phase of a storm when the height reaches to more than 7 km. It contains ice particles transported from neighboring convective areas by wind. The ice particles decrease the 85-GHz brightness temperature. The TMI estimates rain rate from the depression of brightness temperatures over land. Therefore, it is possible that the TMI estimates larger rain rate than the PR for the rain system with large ice particles at the top of cloud when only weak rain exists below the anvil rain, as described in section 3a. Often there is no rain under the anvil rain. Even when the PR determines that it is not raining, the TMI may estimate a significant rain rate, and it is likely that the TMI often overestimates. Because anvil rain usually covers a wide area, the nonuniformity of the field of view is low and a beam-filling effect is small. Other possibilities for the cause of the TMI overestimation will be discussed in section 4.

b. Comparisons over the ocean and coastlines

We focus on rain estimates over land in this paper. It is, however, interesting to compare the rain estimates over the ocean and coastlines. Figure 7 is the same figure as Figs. 2 and 3, but over the ocean and coastlines and only for June 1998. As seen in Fig. 7, over the ocean the TMI-RR is 28% larger than the PR-RR, but the

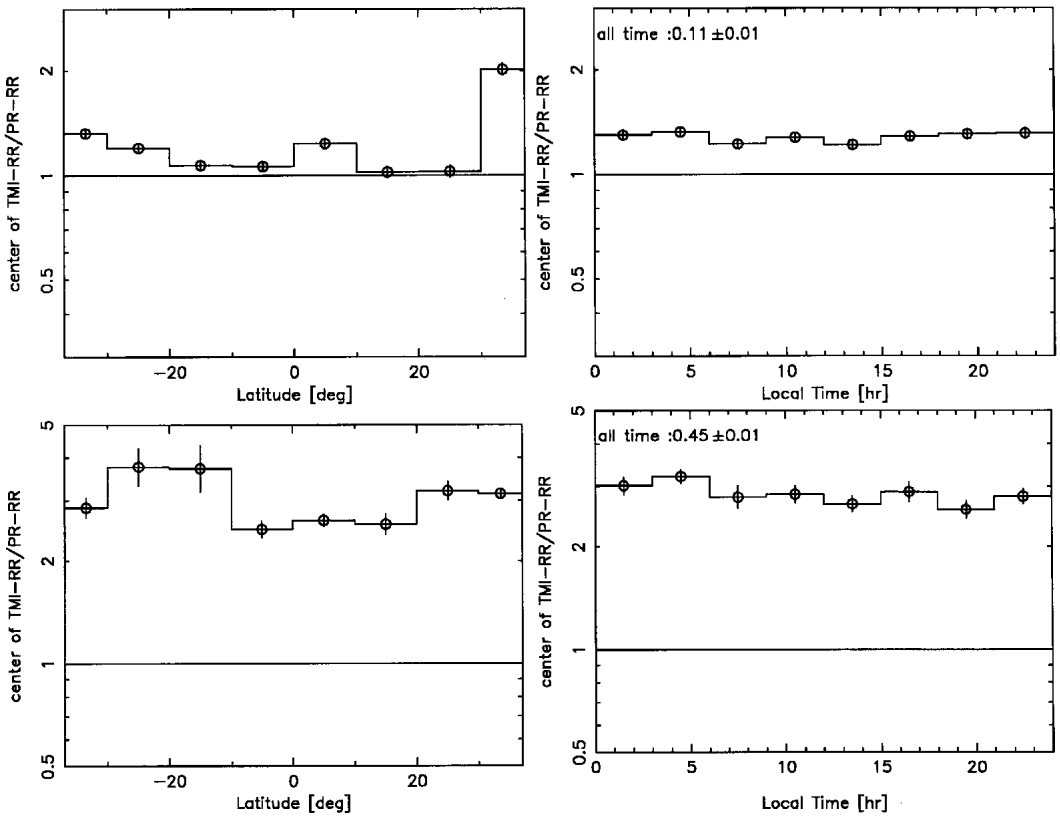

FIG. 7. Same as Figs. 2 and 3 but over (top) the ocean and (bottom) coastlines (Jun 1998 only).

variation with latitude or local time is smaller than over land, except for 30°–37°N. It is not yet clear why the TMI-RR is larger than the PR-RR for that latitude band. Moreover, the TMI is expected to be more reliable over ocean than over land. Therefore, the disagreement between the TMI-RR and PR-RR may be due to PR problems such as the uncertainty in the drop size distribution estimation for oceanic rain performed by the PR rain retrieval algorithm. If so, the uncertainty in the drop size distribution would not depend on the local time and latitude because Fig. 7 shows only small variation with latitude or local time. Moreover, it would also not depend on storm height because of small variation of the relation with storm height, as we describe in a following paragraph. Over coastlines, the TMI-RR is 2.8 times the PR-RR. In particular, the weak rain is overestimated by the TMI (not shown). However, it also lacks in the large variation with local time and latitude. It is possible that this large difference is for the same reasons that the large TMI-RR appears over land, that is, it is suggested that this is due to an anvil rain, evaporation, and/or a tilting system. Another possible suggestion is a principle flaw of the TMI version-5 rain retrieval algorithm over coastlines. This algorithm is based on the SSM/I method of Adler et al. (1993). The brightness temperatures at 37 and 85 GHz are used to define raining areas. The criterion is that 37-GHz brightness temperature is 10 K smaller than 85-GHz brightness temperature. Moreover, the 85-GHz scattering signal is used to assign rain rate through the following equation: 85-GHz brightness temperature = 251.0 − 4.19 (rain rate). In these procedures, only horizontally polarized channels are used. This equation is perhaps not good. The obtained relation between 85-GHz horizontally polarized brightness temperature and TMI-RR over coastlines is tighter than over the ocean and land, showing an almost linear relation (not shown). It can be confirmed that this rain retrieval algorithm is very simple and is not strongly dependent on latitude or characteristics of rain events. This algorithm will mistakenly interpret weak rain (<10 mm h^{-1}) with low optical depth and low 85-GHz brightness temperature from the surface of coastlines (including ocean surface but excluding land surface) to strong rain with strong 85-GHz scattering signal. In regard to the contamination of the emission from the ocean surface due to the low spatial resolution of the TMI footprint or the terrain database used in the algorithm, the effect to the 85-GHz brightness temperature is smaller because the surface temperature is low and similar with the coastlines. On the other hand, the 85-GHz horizontally polarized emission or strong 85-GHz scattering signal from the land surface within a TMI footprint is recognized as weaker or stronger rain, and, then, the result of

TMI overestimation could be derived from the latter strong-scattering case. These effects from land or the ocean are included in the equation used for this algorithm, which was calculated for a tropical squall line case. However, it is not known whether the effects are always sufficiently corrected for global data. Therefore, if the correction of emission contamination from land surface is too large, it is possible that TMI may overestimate the RR because of the contamination.

These effects may give a misleading height of the rain layer. In fact, the rain height expected by the TMI ice and rain profiles is always lower than that obtained by the PR over coastlines. For example, in June of 1998, over coastlines within the latitude of 0°–10°S and the longitude of 90°–135°E, the average PR brightband height and freezing level are 4.46 and 4.81 km, respectively, while the TMI ice content is larger than the TMI water content at a lower altitude of 4 km. It is clear that the TMI underestimates the top height of the rain layer. Over the ocean, the detected emission at the low frequency is approximately proportional to the column-integrated rain, and the rain rate is approximately in inverse proportion to the height of the rain column. Therefore, the TMI underestimation of storm height causes the TMI overestimation of the rain rate near the surface over the ocean. However, the coastline algorithm for rain estimation is more like the land algorithm and uses only 85-GHz horizontally polarized brightness temperature, that is, scattering signal, and so it does not use the rain-layer height like over ocean. The 37-GHz brightness temperature is used only for definition of the raining area over coastlines. Thus, TMI underestimation of the rain-layer height does not affect TMI estimation of RR. However, TMI-RR overestimation seems to underestimate the rain-layer height, although it is still an open question as to why the TMI underestimates the height and how it is associated with an overestimation of RR.

Figure 8 is the same figure as Fig. 4 but for over the ocean and coastlines. Histograms for each storm height over the ocean and coastlines show no prominent variation. That is to say, the relation between the TMI-RR and PR-RR does not strongly depend on the storm height. It is consistent with the fact that diurnal variation of rain systems over the ocean is weak, as shown by Nesbitt and Zipser (2003). Note that the distributions of histograms over the ocean are spread more narrowly than over land and coastlines. However, they have long tails at the lower TMI-RR/PR-RR, when the storm height is less than 4 km. Because PR-2A23 data have a warm-rain flag, we made histograms of certain warm rain and revealed that this tail was caused mainly by the warm, shallow rain (not shown). This result means that rain estimates of warm, shallow rain systems are difficult to make, even over the ocean. The histograms have also small but long tails at the higher TMI-RR/PR-RR when the storm height is larger than 9 km. It is considered that the TMI sometimes overestimates rain rate for deep rain systems, even over the ocean, perhaps because of anvil rain and/or effects of evaporation below the clouds or tilting system. Because this tail is mainly made by weak rain events with a TMI-RR of less than 2 mm h^{-1} (not shown) and the tail is seen uniformly everywhere over the ocean without regard for rain concentration (not shown), this effect is not due to the insufficient attenuation correction of strong rain by the PR algorithm but rather to a beam-filling problem or edge effect of rain systems associated with TMI, and so on. Histograms over coastlines have scattered distributions because of poor sampling and the large uncertainties in the determinations of both the TMI-RR and PR-RR over coastlines. However, it is clear that the TMI frequently estimates a larger rain rate than the PR, perhaps because of a flaw of the retrieval algorithm for the weak rain, the effect of the ocean or land in the footprint of TMI, or the effect of shifted anvil rain.

Thus, the relations between the TMI-RR and PR-RR over the ocean and coastlines are very stable, independent of the storm height, latitude, and local time. On the other hand, over land, there are clear dependencies on storm height as shown in Fig. 4. The dependence of the relation between the TMI-RR and PR-RR on local time as shown in Fig. 3 may be explained by the diurnal variation of a storm height, and the dependence of the relation on the latitude as shown in Fig. 2 is also caused by the meridional variation of storm height.

c. Convective rain

Characteristics as shown in Fig. 4 result mainly from stratiform rain (except for SH >10 km). Histograms of the TMI-RR/PR-RR for convective rain (Fig. 9) have very different distributions, which show that there are many pixels with smaller TMI-RR at any storm height that is less than 10 km. In this figure, pixels with a convective ratio larger than 50% are selected. This ratio is defined as the ratio of the number of convective rain events classified by PR within a grid of $0.2° \times 0.2°$ to the total number of rain events. This figure also shows that the histograms have the same features: the rain with low storm height has smaller TMI-RR and there are tails at the lower TMI-RR/PR-RR. On the other hand, deep convective rain with SH that is greater than 10 km shows minimal bias, which probably indicates that the TMI land algorithm is tuned based on those convective storms with the largest ice-scattering signals. Note that the distributions of stratiform rain with SH that is greater than 10 km are different from Fig. 4 and have large TMI-RR/PR-RR, like the case of SH = 9–10 km in Fig. 4.

Figure 10 is the same as Fig. 6 except that the data are stratified by stratiform rain ratio, defined as the number of stratiform rain events divided by the total number of rain events within a $0.2° \times 0.2°$ grid on an orbit-by-orbit basis. This quantity is almost equal to the complement of the convective rain ratio defined above,

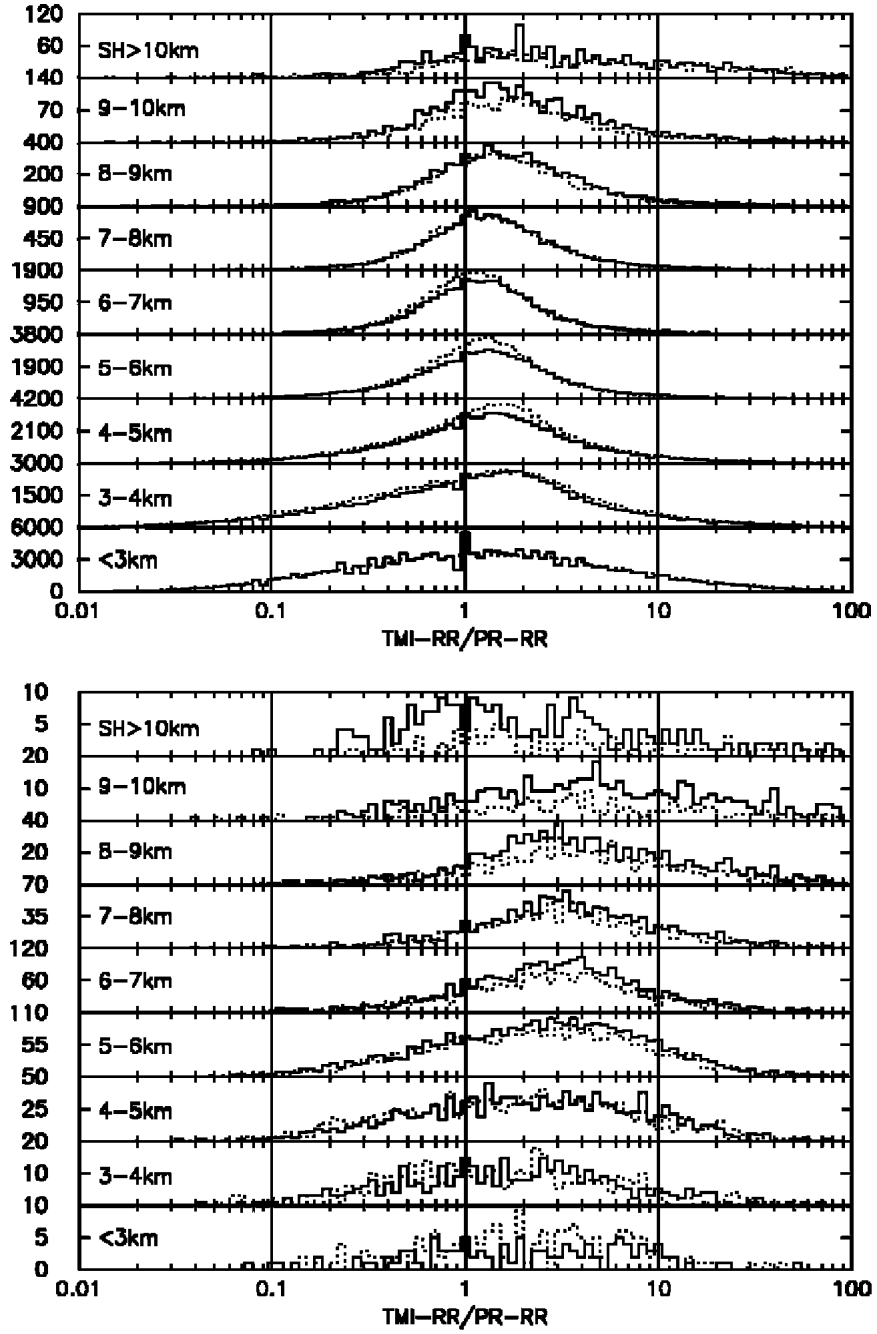

FIG. 8. Same as Fig. 4, but over the (top) ocean and (bottom) coastlines.

because some events classified as "others," which is defined in the TRMM manual (NASA 2000), are rare. For example, grids with an others ratio of larger than 0.1, where a summation of convective and stratiform ratios is smaller than 0.9, are only less than 30% over land. Moreover, it is noted that they are less than 15% over the ocean and less than 20% over coastlines. The left panel of Fig. 10 shows that the stratiform rain ratio is low in the summer and high in the winter. This dependence on the stratiform rain ratio is much smaller than that on the storm height. These results are consistent with Fig. 6. It can be seen in the right panel of Fig. 10 that the stratiform rain ratio is high in the morning (from 0300 to 1200 LT) and low in the afternoon (from 1200 to 2100 LT), which is consistent with Takayabu (2002). This dependence is slightly smaller than that on the storm height. It is also likely to be because convective rain with high storm height frequently develops in

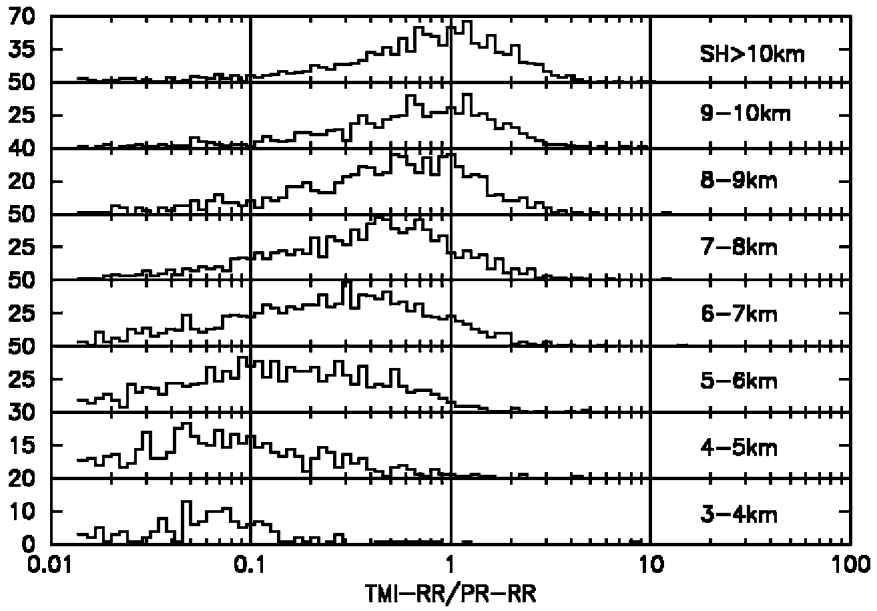

FIG. 9. Same as Fig. 4, but only for convective rain (with PR convective rain ratio of >50%) and only in Jun 1998. The histogram for storm height of <3 km is not shown because there are few events.

the afternoon and does not disappear until morning with a following deep stratiform rain, as shown by Nesbitt and Zipser (2003) and Takayabu (2002). The local time of the high storm height and the high convective ratio, however, shifts by 3 h. This shift means that, after the convective rain is formed, the storm height increases. Although a lower TMI-RR than the PR-RR in Fig. 3 appears from 0600 to 1800 LT, because shallow rain is dominant from 0600 to 1500 LT as shown in Fig. 6, the tendency from 1500 to 1800 LT could not be explained. Now, it is clear that it is caused by pixels with high convective rain ratios. Therefore, the dependencies of the ratio of the TMI-RR to PR-RR on the latitude and local time are due to both shallow rain and convective rain. The effect of a shallow rain seems to be stronger than that of a convective rain. A fraction of the rain amount for each stratiform rain ratio has the same tendency as Fig. 10 (not shown).

Even over the ocean, the relationship between the TMI-RR and PR-RR for convective rain depends on the storm height (Fig. 11). The relationship shows a similar behavior as it does over land. This result may mean that the rain retrieval is difficult for convective rain, because of the large optical thickness, irregular

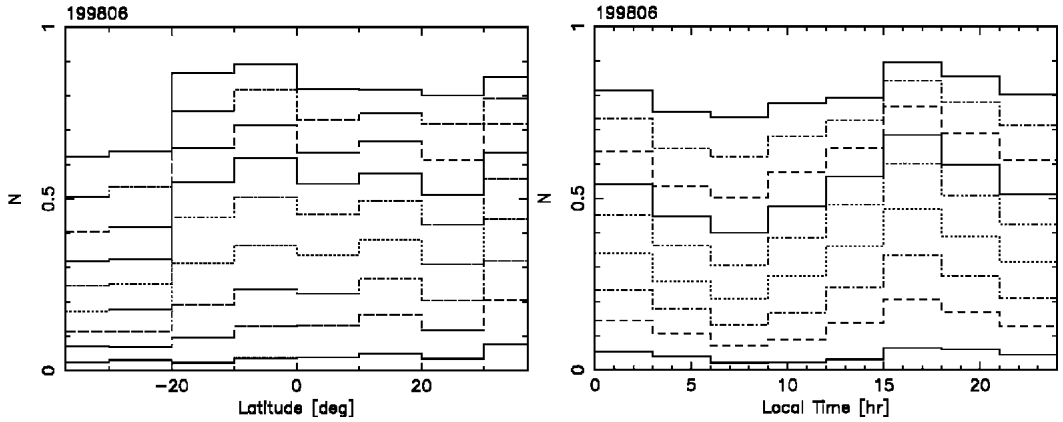

FIG. 10. Fraction of number of rain events with stratiform rain ratio <10% (between zero and the lowest step line), 10%–20% (between the lowest step line and a second lower step line), 20%–30%, 30%–40%, 40%–50%, 50%–60%, 60%–70%, 70%–80%, 80%–90%, and 90%–100% (between the highest step line and unity) over land in Jun 1998: dependence on (left) latitude and (right) local time every 3 h.

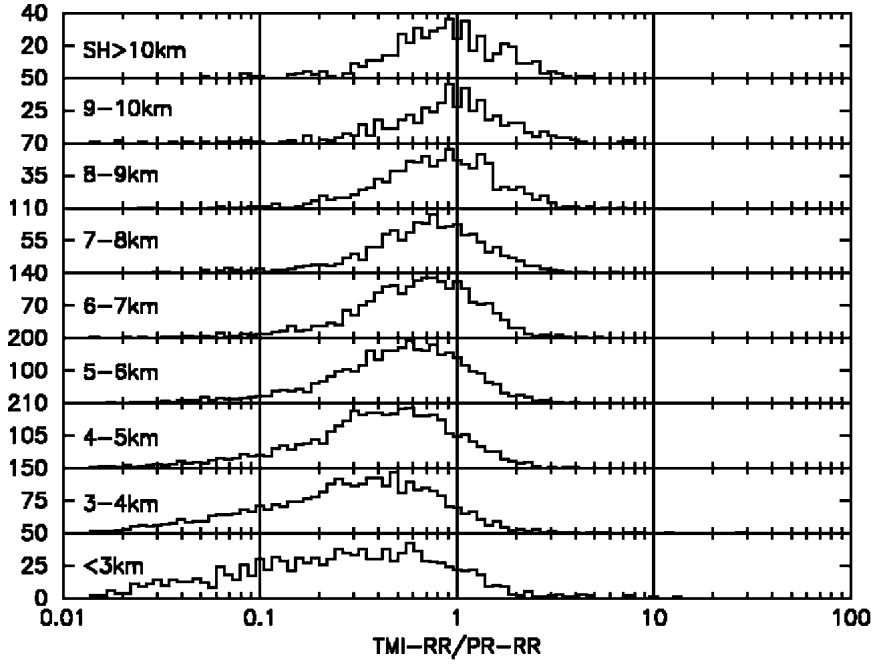

FIG. 11. Same as Fig. 8, but only for convective rain (with PR convective rain ratio of >50%), only in Jun 1998, and over the ocean.

directions of ice particles due to the large turbulence, effect of supercooled water droplets above the freezing level due to the large updraft, or the large beam-filling effect for the case of isolated convective systems, and so on. Over coastlines, the TMI-RR of convective rain with storm height of over 7 km seems to be accidentally consistent with the PR-RR, but the TMI-RR is lower for a shallow rain (not shown). It can be seen that the results for convective and stratiform rain are very different, which implies that a similar algorithm improvement is needed over the ocean, land, and coastlines, but the improvement must be different for each rain type (convective or stratiform rain). On the other hand, the characteristics of stratiform rain are similar to those shown in Figs. 4 and 8, because the stratiform rain occurs much more often than convective rain, which is obvious from the number of events in Figs. 4 and 9 or the upper panels of Figs. 8 and 11. Similar to the upper-left panel of Fig. 7, over the ocean, the TMI-RR for stratiform rain is much larger than the PR-RR in the boreal summer area in the latitude range of 30°–37°N (not shown). This only applies over the ocean.

d. TMI rain detection

Up to this point, we have been discussing the results of a comparison between instantaneous TMI-RR and PR-RR. Next, results pertaining to monthly rain totals are presented. We calculated a PR monthly rain total (RT) PR-RT at each local time at hourly resolution and latitude bins of 37°–30°S, 30°–20°S, 20°–10°S, 10°S–0°, 0°–10°N, 10°–20°N, 20°–30°N, and 30°–37°N, or at all latitudes. At that time, we accumulated the orbital gridded data (0.2° × 0.2°) meeting those conditions. Results of all latitude data for June of 1998 are shown by open circles in Fig. 12. Pixels with zero rain rate were taken into account in making grid maps. Crosses in this figure show the PR rain amount accumulated for pixels with the TMI-RR that is larger than zero. Therefore, the difference between open circles and crosses shows PR

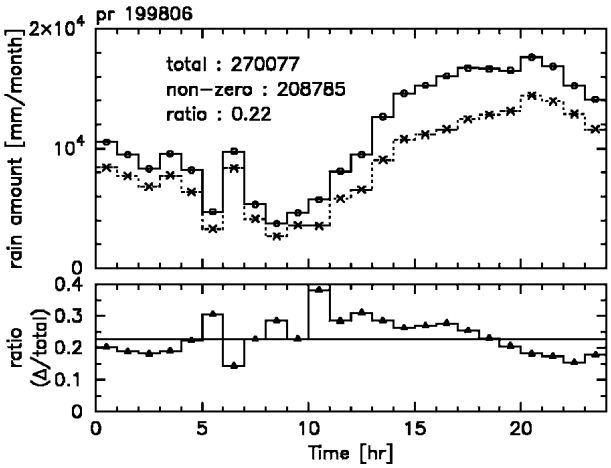

FIG. 12. Dependence of the PR monthly rain total PR-RT on local time over land (open circles and solid step lines) in Jun 1998. Crosses and dotted step lines are for PR monthly rain amount with a TMI rain rate >0. Open triangles and solid step lines show the ratios of monthly rain amount for pixels without a significant TMI rain rate to the monthly rain total, and the line shows the ratio averaged through the day.

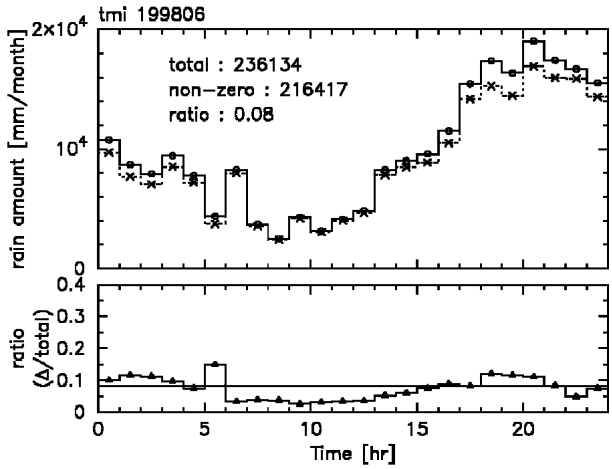

FIG. 13. Dependence of the TMI monthly rain total TMI-RT on local time over land (open circles and solid step lines) in Jun 1998. Crosses and dotted step lines are for TMI monthly rain amount with a PR rain rate >0. Open triangles and solid step lines show the ratios of monthly rain amount for pixels without a significant PR rain rate to the monthly rain total, and the line shows the ratio averaged through a day.

monthly rain amount when the TMI-RR is zero. The ratio of PR rain amount accumulated for pixels with zero TMI-RR to the total [corresponding to (circle − cross)/circle in this figure] is shown by the open triangles in the lower panel of Fig. 12. The ratios are about 10%–30%, except for small rain amounts. The smaller the rain amount is, the larger the ratio is. In winter, the ratio is also large. It may be caused by the poor sensitivity of TMI for shallow rain with a low rain rate. Although figures for each latitude bin are not shown, the zonal region of 0°–10°N has the smallest ratio:10%. In this latitude band, the ratio is large in the daytime (from 1000 to 1400 LT) and small at night (from 2000 to 0500 LT). This result indicates that the TMI detects rain at night more completely than in the daytime. This behavior is consistent with Fig. 3. From December to February, the ratios are less than 20%, except for winter regions in the range of 10°–37°N. The zonal region of 0°–10°S has the smallest ratio—10%.

For comparison, we calculated TMI monthly rain totals TMI-RT for both zero or nonzero PR-RR. The results for June 1998 are shown in Fig. 13. As seen from this figure, the differences between open circles and crosses are much smaller than in Fig. 12 (which is also seen for each latitude band except for 30°–37°N, not shown). The ratios are a few percent or less, except for regions with a small rain amount and the band of 30°–37°N. From December to February, the ratios are also only a few percent, except for the 20°–37°N band. These results suggest that the TMI does not detect rain better than the PR. According to Fig. 4, it may be because shallow rain is not detected by the TMI. To confirm this idea, we made histograms of the PR-RR for pixels with zero TMI-RR and those of the TMI-RR for pixels with zero PR-RR, which are shown in the left panel of Fig. 14. This panel shows that pixels with zero rain rate from one sensor tend to have low rain rates of less than 1 mm h^{-1} from the other. In the right panel of Fig. 14, we show the ratio of these histograms in the left panel to the histograms of total rain observations for each sensor. It can be seen that for the lowest category of nonzero PR-RRs ($0 <$ PR-RR < 1 mm h^{-1}), the fraction of TMI pixels for which the TMI-RR is zero exceeds one-half of the total number of TMI pixels for that PR-RR category. Therefore, the results shown in Fig. 12 can be explained by the low sensitivity of TMI to weak rain. On the other hand, over the zonal region of 30°–37°N (all seasons), the TMI monthly rain total TMI-RT for zero PR-RR is higher (up to 20%) (not shown), perhaps because PR is missing as a result of clutter.

Figure 15 shows diurnal variations of the accumulated rain of PR and TMI. The data shown in this figure are the same as the open circles shown in Figs. 12 and 13. In Fig. 15, the accumulated rain also shows that the TMI-RT is smaller than the PR-RT from 0900 to 1800 LT. This pattern is due to rain events with storm heights of less than 7 km. In the latitudes of 0°–10°N and 30°–37°N, the TMI-RT is larger than PR-RT in the evening, but not if the storm height is less than 6 km (not shown). For the period of December 1998–February 1999, the same tendency is found for 10°S–10°N. These results are consistent with the fact that the TMI underestimates the rain rate of shallow developing convective systems in the afternoon and the TMI overestimates the rain rate of stratiform rain systems around developed convective rain systems with high storm height in the evening. On the other hand, the TMI-RT (shown by circles in Figs. 13 and 15) is nearly equal to the PR-RT, only with nonzero TMI-RR as shown by crosses in Fig. 12. This result implies that a main source of diurnal-variation difference as shown in Fig. 15 is not from TMI rain estimation but TMI detection. That is, TMI rain estimation is not so bad, once the TMI detects rain systems.

Moreover, when the rain rate is larger than 0.7 mm h^{-1}, the correlation in the 30°–37°N band has the same tendency but is more consistent (not shown), which means that the effect of the TMI overestimating weak rain of less than 0.7 mm h^{-1} is large in this band. Note that this consistency of rain amount does not mean consistency at each RR. On the other hand, in the band of 0°–10°N, consistency of the correlation is not improved because many pixels (80%–90%) have PR-RR of >0.7 mm h^{-1}.

4. Discussion

Our results suggest that the TMI overestimates stratiform rain with high storm height from late afternoon to

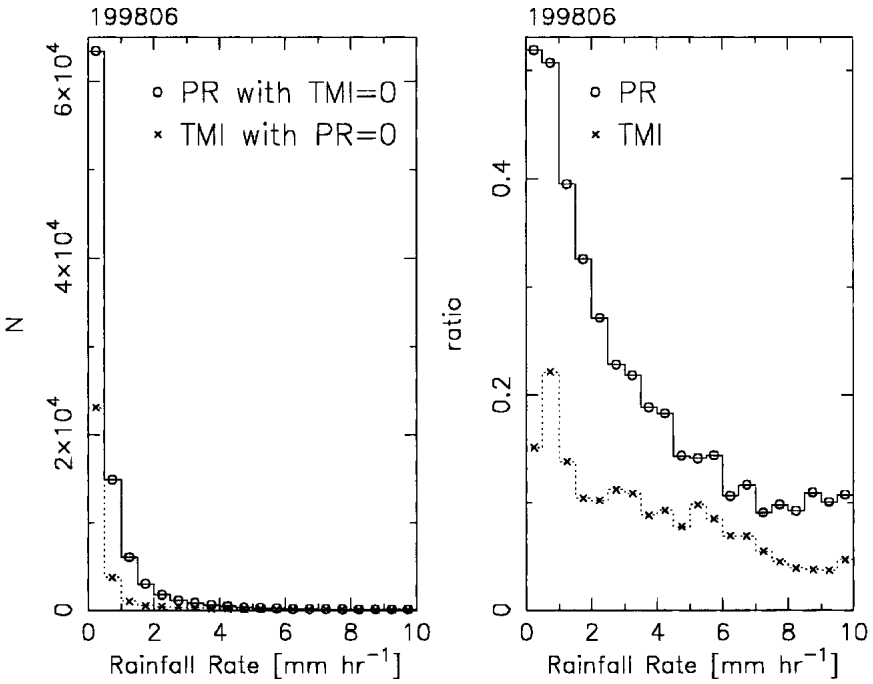

FIG. 14. Histograms of PR-RR with zero TMI-RR (open circles) and TMI-RR with zero PR-RR (crosses) for (left) the rain rate in Jun 1998 and (right) ratios of these to histograms of total PR-RR or total TMI-RR.

night. This overestimation may be caused by the effects of anvil rain with little or no surface rain, evaporation near the surface, or tilting of the storm system. Anvil rain develops in summer and in the Tropics and/or from late afternoon to evening, when there is enough heat to produce a deep storm. The widely spread flat top of a cumulonimbus is formed from the mature stage to the decay phase of a storm, and the height reaches to more than 7 km. It contains ice particles that are transported from neighboring convective areas. The ice particles decrease the brightness temperature observed in the high-frequency channels, that is, at 85 or 37 GHz (Bennartz and Petty 2001). The TMI estimates rain rate from the depression of brightness temperatures over land. Thus, it is probable that the TMI overestimates the rain rate. Fisher (2004) reported a positive TMI afternoon bias relative to the gauges. He suggested that it correlated with the production of ice particles typical of convective systems that form in the afternoon.

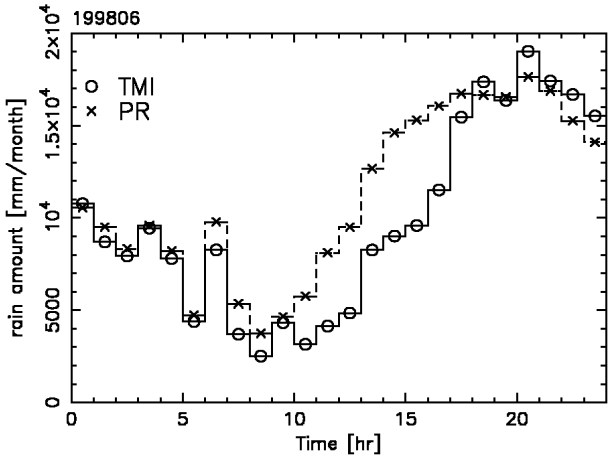

FIG. 15. Dependence of rain amount RT on local time over land in Jun 1998. Open circles show the TMI-RT, and crosses show the PR-RT. The TMI-RT is smaller than PR in the daytime and larger than PR in the late evening, which means that the diurnal variation is different between PR and TMI.

The effect of evaporation appears in a PR profile but is not shown in a TMI profile (as shown in Fig. 16). These contoured-frequency-by-altitude diagrams (CFADs) of rain rate in this figure are accumulated from events with storm heights of 10 ± 0.5 km over land in the band of 0°–10°N. The grayscale is logarithmically spaced. The TMI excludes precipitation ice content above the freezing level. Therefore, the CFAD of the TMI over 6 km should be excluded in the comparison with the PR. For the CFADs with altitude of lower than 3.5 km, the PR rain rate decreases from 4 km to the surface, perhaps due to the effect of evaporation as suggested by Takayabu (2002) and McCollum et al. (2000). On the other hand, the TMI rain rate does not change between 4 km and the surface. As a result, the surface rain rates differ very much and the TMI-RR is much larger than the PR-RR. This condition implies

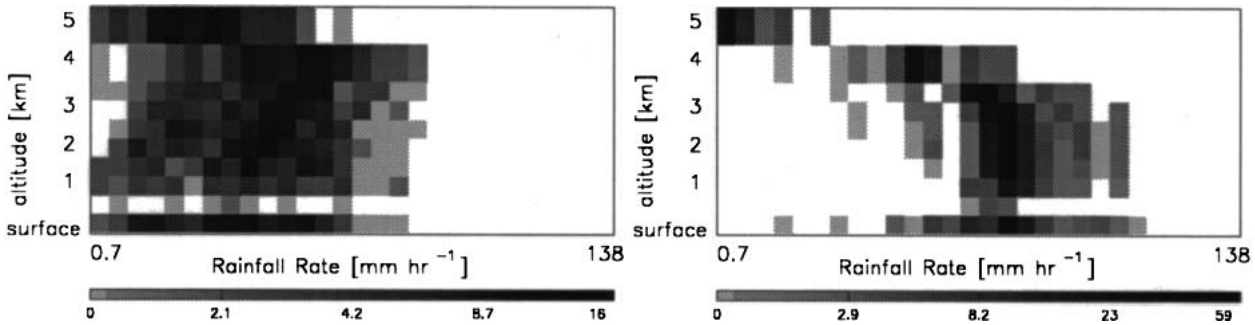

FIG. 16. CFADs of the rain rate of stratiform rain (PR stratiform rain ratio of >80%) with storm height of 10 ± 0.5 km observed with the (left) PR and (right) TMI in Jun 1998. These CFADs are for over land from 0° to 10°N. The grayscale is logarithmically spaced. The lowest grids are for near-surface rain rate; next grids are for 0.5, 1, 1.5, 2, 2.5, 3, 3.5, and 4 km, respectively. The upper grids are for 5 km. For the cases of 4 and 5 km, the grid size of the *y* axis is 2 times that of the other grids. The *x* axis is rain rate logarithmically spaced by a factor of 1.2 from 0.7 to 138 mm h^{-1}. TMI rain rates (mm h^{-1}), except for the surface rain rate, are calculated as 20 times the TMI precipitation water content (PWC; g m^{-3}). The conversion formula from the PWC to RR near the surface is derived by Masunaga et al. (2002).

that the TMI algorithm does not take the effect into account or that the effect used in the algorithm is too weak. This phenomenon makes the TMI rain rate near the surface (i.e., TMI-RR) larger than actual rain rates.

When a storm system tilts (Hong et al. 2000), the difference between the TMI-RR and PR-RR can be large. The TMI detects a depression of the 85-GHz brightness temperature caused by the scattering due to ice particles in the cloud and estimates rain rate. However, the tilting system has no rain in the area below the ice but has rain near the root of the system. For the deep rain system, the PR indicates no precipitation but the TMI shows high scattering signal, especially when the system does not include the root region within the footprint. Thus, the TMI overestimates the near-surface rain rate of the rain system with high storm height. On the other hand, the storm height near the root region is estimated to be low and the root system is classified as a shallow, warm rain if the upper tilting region with the ice layer is out of the TMI footprint. Therefore, TMI overestimation cannot be canceled by cases in which the footprint has surface rain but the path between the satellite and surface misses the rain cloud with ice, because the system is analyzed discretely based on the storm height. All three of these effects cause the TMI overestimation of rain rate for deep rain systems. Moreover, it should be noted that there is an effect of clutter on the PR in the altitude range of 0.5–1.0 km.

Next, we discuss the TMI underestimate for convective rain over land, as shown in Fig. 9. For convective rain with a storm height of less than 9 km, that is, for almost all convective rain systems over land, the TMI-RR is lower than the PR-RR. This tendency is also shown over the ocean or coastlines. We checked the relationship between TMI brightness temperature TMI-Tb_{85GHzV} of vertical polarization at 85 GHz and PR rain rate at 3 km for each SH. Results of SH = 4, 6, and 8 km are shown in Fig. 17. In addition to no significant TMI-Tb_{85GHzV} depressions for shallow convective and stratiform rain (as shown in the left panel of Fig. 17), there are also smaller depressions for convective rain with SH of 6 km than for stratiform rain (as shown in the middle panel of Fig. 17), except some data with very large depression and large PR rain rate. These characteristics are the same over both ocean and land. In general, regardless of surface conditions, for a given PR rain rate, the depression by ice scattering of nonshallow and nondeep convective rain is smaller than that for stratiform rain. In other words, the phenomenon is that, for a given brightness temperature depression, PR rain rate is higher for convective rain than for stratiform rain. This result is consistent with McCollum and Ferraro (2003). It is perhaps because of strong mixing of various particles by strong turbulence. Emission from supercooled water droplets resulting from a strong updraft is added. Only surface information is obtained because of the large optical thickness. Emission from outside of the convective system is included when the convective system is isolated. Therefore, the rain retrieval from the depression of convective storms is difficult. Even over the ocean, it is difficult (as shown in the middle panel of Fig. 17, resulting in Fig. 11). Another possibility of the PR overestimation for convective rain being due to an inappropriate drop size distribution over both land and ocean is also left. In the TRMM standard products, version 6 (McCollum and Ferraro 2003), a convective and stratiform probability will be made for each pixel and the rain rate will be estimated to be higher for a rain event with high convective probability. Therefore, the biases will be improved. On the other hand, the right panel of Fig. 17 has an opposite tendency to the left panel. Deep-convection rain shows a larger depression than stratiform rain, though the deviations are very large. It is thought that this large depression is correctly used for TMI rain retrieval over land and, then, the TMI-RR is derived to be consistent with PR-RR.

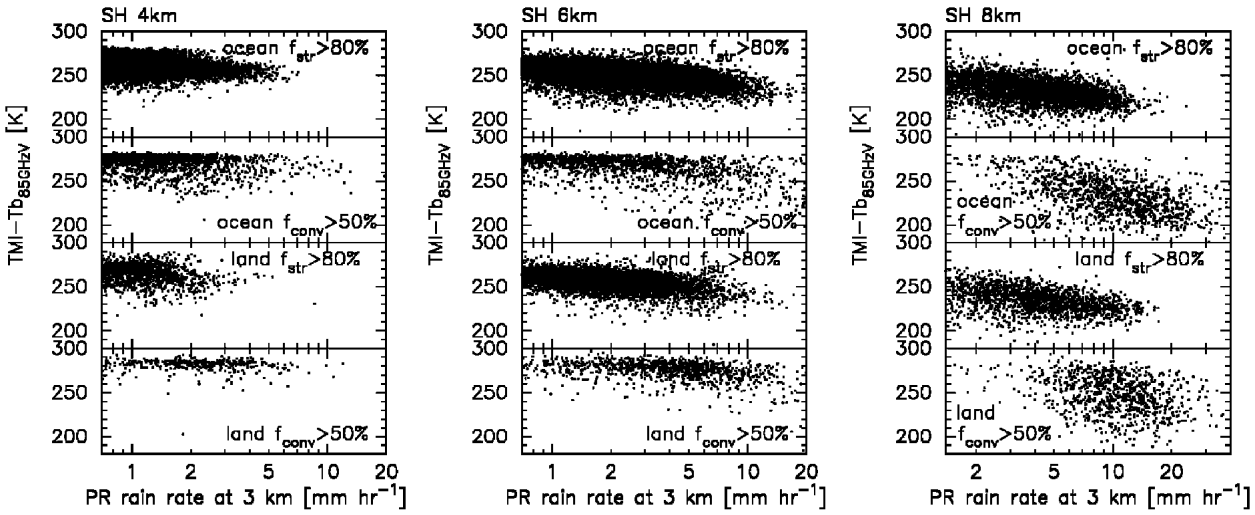

FIG. 17. Correlation of Tb_{85GHzV} and PR rain rate at 3 km for an SH of (left) 4 ± 0.5, (middle) 6 ± 0.5, and (right) 8 ± 0.5 km during Jun 1998. The four panels are for stratiform rain (stratiform rain fraction >80%) over the ocean, for convective rain (convective rain fraction >50%) over the ocean, for stratiform rain over land, and for convective rain over land, respectively. The abscissa is PR rain rate at 3 km, and the ordinate is TMI-Tb_{85GHzV}. The TMI-Tb_{85GHzV} is obtained from the orbital gridded data, which are accumulated from each pass of data in TMI-1B11 with the same procedure as TMI-RR.

For shallow convective systems, the principal reason that TMI underestimates is poor detectability by TMI caused by the lack of solid particles, supported by the left panel in Fig. 17. This fact will occur not only for shallow isolated systems, but also in the root areas of large and deep systems. Because convective rains appear in the first stage of development, rain systems are shallow and have little or no ice particles, making it difficult for the TMI to detect the rain. This is the former case. The latter case is because the view angle of TMI is 53° off nadir and/or the system may be tilted. Even for large developed precipitation systems, if the vertical structure of the systems is tilted, the root areas are shallow. Because of the horizontal shift of the ice layer, the 85-GHz brightness temperature of shallow rain with large rain rates does not decrease. Thus, the TMI underestimates the rain rate.

The possibility that the PR overestimates a rain rate of shallow convective rain must also be considered. The surface reference technique is not well used for this type of rain, because it is hard to estimate a small attenuation exactly for weak rain (Iguchi et al. 2000). Therefore, the validity of used raindrop size distributions is an issue. Viltard et al. (2000) estimated the influence of the drop size distribution on rain retrievals through a radiative transfer simulation and suggested that a crude consistency between the PR and TMI may be achieved if a different distribution is used. A storm-by-storm precise raindrop size distribution will be necessary for a future PR algorithm. Bennartz and Petty (2001) also mentioned that the choice of a suitable Z–R relation for conversion of radar reflectivities to rain rate is important, because an apparent variability of a factor of 6–7 in the relation between scattering index based on ice particle size distribution and rain rate was obtained for the different precipitation events. If the size distribution of each event with different storm height is systematically different, the different biases based on storm height (as seen in Figs. 4, 9, and 11) may be able to be explained. Another possibility is that the attenuation correction for strong convective storms is too large in the PR algorithm. However, deep-convection systems have good correlation (though it might be accidental), and this possibility may be negated.

5. Conclusions

We investigated the relation of the instantaneous near-surface rain rate between the TMI and PR over land and found that it depends on the latitude, local time, storm height, and convective/stratiform rain ratio. The dependencies revealed the weak points of the TRMM algorithm and enabled discussion of the causes. The dependencies are summarized as follows: the TMI-RR is smaller than the PR-RR in winter and/or from 0900 to 1800 LT and/or for storm height lower than 6 km and/or for convective rain. On the other hand, the TMI-RR is larger than the PR-RR in summer and/or at night and/or for storm height higher than 6 km and/or for stratiform rain.

According to these dependencies, it is clear that the TMI has difficulty detecting shallow rain in the early developing stage, which appears in the afternoon, especially a shallow convective rain. It is perhaps due to little or no ice scattering, though the possibility of problems on particle size distribution is left. On the other

hand, the TMI overestimates deep stratiform rain with a widespread anvil around strong, deep convective rain in the mature stage and the decay phase because of the effects of an anvil rain with a little or no surface rain, evaporation near the surface, or tilting of the storm system.

Moreover, the ratio of a PR rain with zero TMI-RR is about 10%–30%, whereas the ratio of a TMI rain with zero PR-RR is only a few percent. These results are thought to be mainly due to the limitation of the TMI detection capability. Therefore, we have to be careful in using the TMI-RR data over land to study the diurnal variation or for regional comparison.

The TMI-RR of convective rain with storm height of less than 10 km is underestimated over land. Similar tendencies are obtained for convective rain over ocean and coastlines. Therefore, similar kinds of improvement for the TRMM algorithm are needed over land. However, an expected improvement apparently is different for convective rain and stratiform rain.

Acknowledgments. We thank Professor T. T. Wilheit for his many useful comments and his help in improving the English expression of the manuscript. We also thank all of the members of the TRMM team in NASA and JAXA for their operation of the satellite and for providing data. This work was supported by the Japan Science and Technology Corporation (JST) and JAXA.

REFERENCES

Adler, R. F., A. J. Negri, P. R. Keehn, and I. M. Hakkarinen, 1993: Estimation of monthly rainfall over Japan and surrounding waters from a combination of low-orbit microwave and geosynchronous IR data. *J. Appl. Meteor.,* **32,** 335–356.

Bennartz, M. D., and G. W. Petty, 2001: The sensitivity of microwave remote sensing observations of precipitation to ice particle size distributions. *J. Appl. Meteor.,* **40,** 345–364.

Ferraro, R. R., 1997: Special Sensor Microwave Imager derived global rainfall estimates for climatological applications. *J. Geophys. Res.,* **102**, 16 715–16 735.

Fisher, B. L., 2004: Climatological validation of TRMM TMI and PR monthly rain products over Oklahoma. *J. Appl. Meteor.,* **43,** 519–535.

Hitschfeld, W., and J. Bordan, 1954: Errors inherent in the radar measurement of rainfall at attenuating wavelengths. *J. Atmos. Sci.,* **11,** 58–67.

Hong, Y., J. L. Haferman, W. S. Olson, and C. Kummerow, 2000: Microwave brightness temperatures from tilted convective systems. *J. Appl. Meteor.,* **39,** 983–998.

Iguchi, T., T. Kozu, R. Meneghini, J. Awaka, and K. Okamoto, 2000: Rain-profiling algorithm for the TRMM precipitation radar. *J. Appl. Meteor.,* **39,** 2038–2052.

Ikai, J., and K. Nakamura, 2003: Comparison of rain rates over the ocean derived from TRMM Microwave Imager and precipitation radar. *J. Atmos. Oceanic Technol.,* **20,** 1709–1726.

Kummerow, C., and L. Giglio, 1994: A passive microwave technique for estimating rainfall and vertical structure information from space. Part I: Algorithm description. *J. Appl. Meteor.,* **33,** 3–18.

——, W. Barnes, T. Kozu, J. Shiue, and J. Simpson, 1998: The Tropical Rainfall Measuring Mission (TRMM) sensor package. *J. Atmos. Oceanic Technol.,* **15,** 809–817.

——, and Coauthors, 2000: The status of the Tropical Rainfall Measuring Mission (TRMM) after two years in orbit. *J. Appl. Meteor.,* **39,** 1965–1982.

——, and Coauthors, 2001: The evolution of the Goddard Profiling Algorithm (GPROF) for rainfall estimation from passive microwave sensors. *J. Appl. Meteor.,* **40,** 1801–1820.

Masunaga, H., T. Iguchi, R. Oki, and M. Kachi, 2002: Comparison of rainfall products derived from TRMM Microwave Imager and precipitation radar. *J. Appl. Meteor.,* **41,** 849–862.

McCollum, J. R., and R. R. Ferraro, 2003: Next generation of NOAA/NESDIS TMI, SSM/I, and AMSR-E microwave land rainfall algorithms. *J. Geophys. Res.*, **108,** 8382, doi:10.1029/2001JD001512.

——, A. Gruber, and M. B. Ba, 2000: Discrepancy between gauges and satellite estimates of rainfall in equatorial Africa. *J. Appl. Meteor.,* **39,** 666–679.

Meneghini, R., T. Iguchi, T. Kozu, L. Liao, K. Okamoto, J. A. Jones, and J. Kwiatkowski, 2000: Use of the surface reference technique for path attenuation estimates from the TRMM precipitation radar. *J. Appl. Meteor.,* **39,** 2053–2070.

NASA, 2000: Tropical Rainfall Measuring Mission science data and information system: File specifications for TRMM products—Level 2 and level 3. National Aeronautics and Space Administration, Goddard Space Flight Center, 83 pp.

Nesbitt, S. W., and W. J. Zipser, 2003: The diurnal cycle of rainfall and convective intensity according to three years of TRMM measurements. *J. Climate,* **16,** 1456–1475.

Short, D. A., and K. Nakamura, 2000: TRMM radar observations of shallow precipitation over the tropical oceans. *J. Climate,* **13,** 4107–4124.

Simpson, J., R. F. Adler, and F. R. North, 1988: A proposed Tropical Rainfall Measuring Mission (TRMM) satellite. *Bull. Amer. Meteor. Soc.,* **69,** 278–295.

Spencer, R. W., 1986: A satellite passive 37-GHz scattering-based method for measuring oceanic rain rates. *J. Climate Appl. Meteor.,* **25,** 754–766.

——, H. M. Goodman, and R. E. Hood, 1989: Precipitation retrieval over land and ocean with the SSM/I: Identification and characteristics of the scattering signal. *J. Atmos. Oceanic Technol.,* **6,** 254–273.

Takayabu, Y. N., 2002: Spectral representation of rain profiles and diurnal variations observed with TRMM PR over the equatorial area. *Geophys. Res. Lett.,* **29,** 1584, doi:10.1029/2001GL014113.

Viltard, N., C. Kummerow, W. S. Olson, and Y. Hong, 2000: Combined use of the radar and radiometer of TRMM to estimate the influence of drop size distribution on rain retrievals. *J. Appl. Meteor.,* **39,** 2103–2114.